Astronomy & Astrophysics

PACS Evolutionary Probe (PEP) – A *Herschel* key program[*]

D. Lutz[1], A. Poglitsch[1], B. Altieri[2], P. Andreani[3,4], H. Aussel[5], S. Berta[1], A. Bongiovanni[6,7], D. Brisbin[8], A. Cava[12], J. Cepa[6,7], A. Cimatti[9], E. Daddi[5], H. Dominguez-Sanchez[9], D. Elbaz[5], N. M. Förster Schreiber[1], R. Genzel[1], A. Grazian[10], C. Gruppioni[9], M. Harwit[8], E. Le Floc'h[5], G. Magdis[5], B. Magnelli[1], R. Maiolino[10], R. Nordon[1], A. M. Pérez García[6,7], P. Popesso[1], F. Pozzi[9], L. Riguccini[5], G. Rodighiero[11], A. Saintonge[1], M. Sanchez Portal[2], P. Santini[10,1], L. Shao[1], E. Sturm[1], L. J. Tacconi[1], I. Valtchanov[2], M. Wetzstein[1], and E. Wieprecht[1]

[1] MPE, Postfach 1312, 85741 Garching, Germany
  e-mail: lutz@mpe.mpg.de
[2] European Space Astronomy Centre, Villafranca del Castillo, Spain
[3] European Southern Observatory, Karl-Schwarzschild-Straße 2, 85748 Garching, Germany
[4] INAF - Osservatorio Astronomico di Trieste, via Tiepolo 11, 34143 Trieste, Italy
[5] IRFU/Service d'Astrophysique, Bât. 709, CEA-Saclay, 91191 Gif-sur-Yvette Cedex, France
[6] Instituto de Astrofísica de Canarias, 38205 La Laguna, Spain
[7] Departamento de Astrofísica, Universidad de La Laguna, Spain
[8] Space Science Building, Cornell University, Ithaca, NY 14853-6801, USA
[9] Istituto Nazionale di Astronomia, Osservatorio Astronomico di Bologna, via Ranzani 1, 40127 Bologna, Italy
[10] INAF – Osservatorio Astronomico di Roma, via di Frascati 33, 00040 Monte Porzio Catone, Italy
[11] Dipartimento di Astronomia, Universitá di Padova, 35122 Padova, Italy
[12] Departamento de Astrofísica, Facultad de CC. Físicas, Universidad Complutense de Madrid, 28040 Madrid, Spain

Received 19 April 2011 / Accepted 9 June 2011

ABSTRACT

Deep far-infrared photometric surveys studying galaxy evolution and the nature of the cosmic infrared background are a key strength of the *Herschel* mission. We describe the scientific motivation for the PACS Evolutionary Probe (PEP) guaranteed time key program and its role within the entire set of *Herschel* surveys, and the field selection that includes popular multiwavelength fields such as GOODS, COSMOS, Lockman Hole, ECDFS, and EGS. We provide an account of the observing strategies and data reduction methods used. An overview of first science results illustrates the potential of PEP in providing calorimetric star formation rates for high-redshift galaxy populations, thus testing and superseding previous extrapolations from other wavelengths, and enabling a wide range of galaxy evolution studies.

Key words. surveys – galaxies: evolution – galaxies: active – infrared: galaxies

1. Motivation

Over the past two decades, it has become increasingly clear that no understanding of galaxy evolution can be obtained without accounting for the energy that is absorbed by dust and re-emitted at mid- and far-infrared wavelengths. For example, early attempts to reconstruct the cosmic star formation history suffered from uncertainties in the obscuration corrections that have to be applied to the rest frame ultraviolet measurements (e.g., Madau 1996; Lilly et al. 1996). Soon, the importance of luminous dusty high-redshift galaxies was highlighted by the detection of infrared-luminous populations both in the mid-infrared (e.g., Aussel et al. 1999; Genzel & Cesarsky 2000) and the submm (e.g., Hughes et al. 1998). Mainly thanks to the large mid-infrared legacy that the *Spitzer* mission provided for extragalactic studies (Soifer et al. 2008), a global consistency between these two perspectives from the rest frame ultraviolet and from the rest frame mid-IR side could be achieved (e.g., Hopkins & Beacom 2006). This is because the rest frame ultraviolet

obscuration on average can be constrained by comparing the observed ultraviolet emission to the sum of ultraviolet and infrared emission. Extrapolation from the mid-infrared to the rest far-infrared was still necessary, however, on the basis of SED assumptions that were untested at the redshifts to which they had to be applied.

At the same time, the detection of the cosmic far-infrared background (CIB) with total energy content similar to the optical/near-infrared one (Puget et al. 1996; Hauser et al. 1998) highlighted the importance of dust emission in the cosmic energy budget. An increase with redshift in the energy output of dusty galaxies relative to others was inferred both from the shape of the CIB and from the more rapid increase with redshift of IR energy density compared to ultraviolet energy density in the resolved observations (e.g., Le Floc'h 2005). All these lines of evidence strongly suggest that our picture of high-redshift galaxy evolution is substantially incomplete and emphasize the need for direct rest frame "calorimetric" far-infrared measurements of individual high-z galaxies, in order to avoid SED extrapolation and to increasingly replace population averages with individual measurements. While small cryogenic space telescopes like *ISO* and *Spitzer* were already equipped with sensitive far-infrared

---

[*] *Herschel* is an ESA space observatory with science instruments provided by European-led Principal Investigator consortia and with important participation from NASA.

detectors, they were for these wavelengths rapidly limited by source confusion, and thus focussed on the study of local objects, or at $z \gtrsim 0.5$ on study of only the most luminous galaxies. They also were able to resolve only a small fraction of the cosmic infrared background.

With ESA's *Herschel* space observatory (Pilbratt 2010) and its PACS (Poglitsch et al. 2010) and SPIRE (Griffin et al. 2010) instruments, this has changed dramatically. With its 3.5 m passively cooled mirror it provides the much improved spatial resolution (thus reduced source confusion) and the sensitivity needed for the next significant step in far-infrared studies of galaxy evolution. Members of the PACS instrument consortium, the *Herschel* Science Centre, and mission scientist M. Harwit have joined forces in the *PACS Evolutionary Probe (PEP)* deep extragalactic survey to make use of this opportunity. PEP aims to resolve the cosmic infrared background and determine the nature of its constituents, determine the cosmic evolution of dusty star formation and of the infrared luminosity function, elucidate the relation of far-infrared emission and environment, and determine clustering properties. Other main goals include study of AGN/host coevolution, and determination of the infrared emission and energetics of known high-redshift galaxy populations.

PEP encompasses deep observations of blank fields and lensing clusters, close to the *Herschel* confusion limit, in order to probe down to representative high-redshift galaxies, rather than being restricted to individually interesting extremely luminous cases. PEP is focused on PACS 70, 100, and 160 μm observations. SPIRE observations of the PEP fields are obtained in coordination with PEP by the HerMES survey (Oliver et al. 2011). Larger and shallower fields are observed by HerMES (70 deg^2), as well as by the H-ATLAS survey (570 deg^2, Eales et al. 2010), while the GOODS-*Herschel* program (Elbaz et al. 2011) provides deeper observation in (part of) the GOODS fields that are also covered by PEP. Finally, the *Herschel* lensing survey (Egami et al. 2010) substantially increases the number of lensing clusters observed with *Herschel*, adding about 40 clusters to the 10 objects covered by PEP. Figure 1 compares the area and exposure of the PEP surveys for 160 μm wavelength (Table 1) with that of these other major *Herschel* extragalactic surveys. An exposure of 1000 s here corresponds to an approximate 3σ depth of 8 mJy. Scaling this as exposure$^{-0.5}$ to smaller/deeper fields will be too optimistic because of increasing overhead fractions and beginning source confusion.

In this paper, we describe the field selection, observing strategy, and data analysis methods of PEP. We give a complete overview of the planned PEP observations and their execution status as of June 2011 (Table 1). We provide a detailed account of the science demonstration phase (SDP) data sets for GOODS-N and Abell 2218, and give an overview of first science results.

2. Field selection

A key element in selecting a field for a deep *Herschel* extragalactic survey is the availability of a strong multiwavelength database from X-rays to radio wavelengths, which is fundamental to many of the science results discussed in Sect. 6. In particular, deep optical, near-IR, and Spitzer imaging, as well as a comprehensive set of photometric and spectroscopic redshifts are essential assets for most of the far-infrared studies of galaxy evolution that we envisage. Deep X-ray data are invaluable for using the potential of *Herschel* for studying the AGN – host galaxy coevolution.

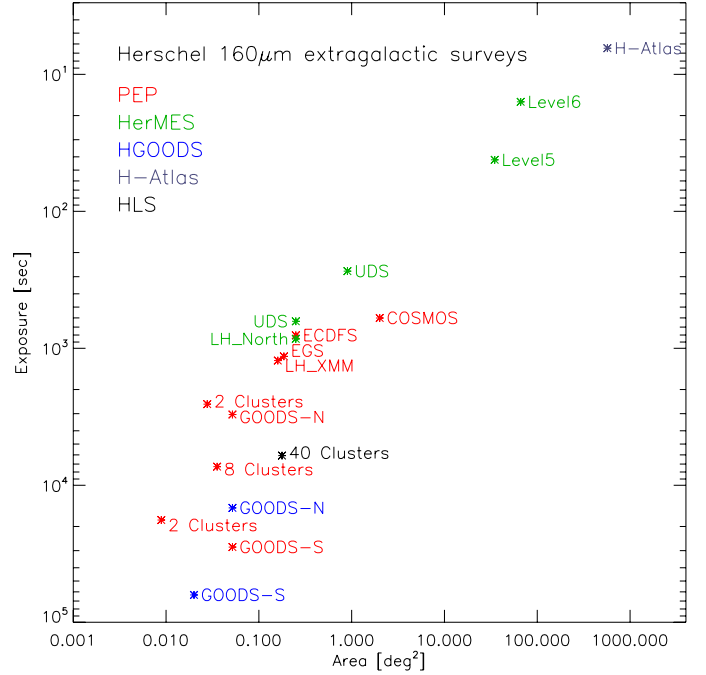Another requirement is a low galactic far-infrared background in order to minimize contamination by galactic "cirrus"

Fig. 1. Area and 160 μm exposure of PEP surveys (red) compared to other major *Herschel* extragalactic surveys. Exposure is defined as survey time (including overheads) multiplied by the ratio of PACS array size and survey area.

structure and by individual galactic foreground objects. This naturally coincides with the selection criteria of extragalactic surveys at other wavelengths. In the X-ray regime, for example, these are pushing for a low galactic foreground obscuration. Given that the power spectra of far-infrared emission of galactic cirrus are steeply decreasing towards higher spatial frequencies (e.g., Kiss et al. 2001), such cirrus contamination is much less of a practical worry for point source detection in deep *Herschel* fields than for the previous smaller cryogenic space telescopes. In any case, our blank field selection includes some of the lowest galactic foreground fields (Lockman Hole, CDFS, 100 μm sky brightness $\sim$0.4 MJy/sr), reaching up to $\sim$0.9 MJy/sr (COSMOS). Our individual cluster fields typically show a 100 μm galactic foreground of 1–2 MJy/sr, with a maximum of 4.5 MJy/sr (Abell 2390).

Our largest field is the contiguous 2 square degree COSMOS (Scoville et al. 2007) observed for about 200 h to a 3σ depth at 160 μm of 10.2 mJy. At this level, integral number counts reach one source per 24 beams (Berta et al. 2010, 2011), similar to the 5σ 40 beams/source definition of the "confusion limit" used by, e.g., Rowan-Robinson et al. (2001). Slightly deeper observations have been obtained for the Lockman Hole (e.g., Hasinger et al. 2001), the Extended Groth Strip EGS covered by the Aegis survey (Davis et al. 2007), and the extended *Chandra* Deep Field South (ECDFS) for which the name has been coined in X-rays (Lehmer et al. 2005), but a multitude of data exist at other wavelengths. Refined analysis of source confusion (Dole et al. 2004) suggests that with the 100 μm and 160 μm number counts turning over at a depth that is reached with PEP (Berta et al. 2010, 2011), deeper observations can still be extracted reliably, in particular when using position priors from very deep 24 μm data (e.g., Magnelli et al. 2009). We make use of this in our deepest blank field observations, which are centered on the GOODS fields (Dickinson et al., in prep.), with strong emphasis on the GOODS-S. GOODS-S also is the only field that we also

Table 1. PEP fields.

Field	RA	Dec	Size	PA	Wavelengths	Observations	Time
	degree, J2000		arcmin	degree	μm		h
COSMOS	150.11917	2.20583	85×85	0^a	$100,160^b$	Nov. 2009–Jun. 2010	196.9
Lockman Hole XMM	163.17917	57.48000	24×24	0	$100,160^b$	Oct. 2009–Nov. 2009	32.1
EGS	214.82229	52.82617	67×10	40.5	$100,160^b$	May 2011–June 2011	34.8
ECDFS	53.10417	–27.81389	30×30	0	$100,160^b$	Feb. 2010–Feb. 2011	32.8
GOODS-S	53.12654	–27.80467	17×11	–11.3	$70,100,160^b$	Jan. 2010	239.7
GOODS-N	189.22862	62.23867	17×11	41	$100,160^b$	Oct. 2009	25.8
Cl0024+16	6.62500	17.16250	6×6	45^c	$100,160^b$	Jun. 2010	6.2
Abell 370	39.97083	–1.57861	4×4	45^c	$100,160^b$		5.3
MS0451.6-0305	73.55000	–3.01667	4×4	45^c	$100,160^b$	May 2010	5.3
Abell 1689	197.87625	–1.34000	4×4	45^c	$100,160^b$	Jan. 2011–	13.0
RXJ1347.5-1145	206.87708	–11.75250	4×4	45^c	$100,160^b$	Feb. 2011	5.3
MS1358.4+6245	209.97625	62.51000	4×4	45^c	$100,160^b$	May 2010	5.3
Abell 1835	210.25833	2.87889	4×4	45^c	$100,160^b$	Feb. 2011	5.3
Abell 2218	248.97083	66.20611	4×4	45^c	$100,160^b$	Oct. 2009	10.2
Abell 2219	250.08333	46.71194	4×4	45^c	$100,160^b$	May 2010	5.3
Abell 2390	328.40417	17.69556	4×4	45^c	$100,160^b$	May 2010	5.3
RXJ0152.7-1357	38.17083	–13.96250	10×5	45	100,160,250,350,500	Mar. 2010–Jan. 2011	5.8
MS1054.4-0321	164.25092	–3.62428	10×5	0	100,160,250,350,500	Jun. 2010–Dec. 2010	5.8

Notes. List of the six blank deep fields, ten lensing clusters, and two $z \sim 1$ clusters to be observed by PEP. As of early June 2011, surveys for all fields except Abell 370 and Abell 1689 are completed (see column "Observations"). [a] Approximate. See Sect. 3 for detailed implementation; [b] 250, 350, 500 μm obtained in coordinated observations by the HerMES key program (Oliver et al. 2011); [c] in array coordinates, true position angle on sky will depend for these fields on execution date of the observation.

observe at 70 μm, to a depth where *Spitzer*/MIPS would be confused. For redshifts around 1, our blank field observations sample a range of environments from the field to moderately massive clusters, which are known in particular in COSMOS due to its large angular size but still excellent multiwavelength characterization. To extend this to the full range of environments at this redshift, we add dedicated observations of two of the best-studied massive $z \sim 1$ clusters, RXJ0152.7-1357 (e.g., Ebeling et al. 2000) and MS1054.4-0321 (e.g., Tran et al. 1999).

We use the amplification provided by massive galaxy clusters to study sources that would otherwise be too faint for direct observations even in our deepest blank fields, and to provide highest quality SEDs on more luminous objects that are also detectable in the blank fields. For that purpose, we have selected ten of the best-studied lensing clusters at redshifts $z \sim 0.2$–0.5. With a 4′ size our observations for these fields are optimized for studying lensed background objects. They will also detect part of the cluster members from the central region, but not the cluster outskirts and the adjacent field population.

Main parameters of our survey fields are summarized in Table 1. Field sizes are quoted there in terms of the nominal scan length. Given the 3.5′×1.75′ size of the PACS arrays, coverage is unequal at the field edges starting to decrease already inside the quoted fields, but also extending beyond them. Observing times are as computed in HSPOT 5.2, true execution times can differ due to overhead changes during the *Herschel* mission.

3. Observing strategy

The scan map is the PACS photometer observing mode that is best suited to getting deep maps close to the confusion limit, for regions that are dominated by (almost) point sources. During a PACS prime-mode, scan map observation, the telescope moves back and forth in a pattern of parallel scan lines that are connected by short turnaround loops. During such a scan, the PACS photometer arrays take data samples at 10 Hz frequency. Given

the presence of 1/f noise in the PACS bolometers, we consistently follow the recommendation to adopt a medium scan speed of 20 arcsec/s that reduces the effects of 1/f noise on point source sensitivity compared to a slow scan speed of 10 arcsec/s, while not yet causing the point spread function (PSF) degradation that is present in fast scans at 60 arcsec/s because of data sampling and detector time constants.

Much of the science from deep far-infrared surveys strongly benefits from the availability of ancillary multiwavelength data that have historically been obtained in fields of a certain shape and orientation. We have matched our blank field data to such constraints (e.g., the shape/orientation of the mid-IR GOODS fields) by typically defining scan layouts in "sky" coordinates rather than "array" coordinates that rotate with epoch of observation. This also facilitates the combination of data from different epochs. Exceptions to this approach are the COSMOS field (discussed below) and the small lensing cluster fields for which there is no preferred orientation.

Reaching the desired depths for our fields requires multiple passages over a given point in the sky. Rather than simply repeating a single scan, we use this to improve the redundancy of the data. Specifically, the observation setup for PEP includes

– Scans in both nominal and orthogonal directions. While the highpass-filtered data reduction discussed in Sect. 4 does not require this, this crosslinking is essential for alternative reductions with full inversion algorithms such as the MadMap implementation in the *Herschel* Common Science System (HCSS)[1] software environment. Typically, we obtain the same number of astronomical observing requests (AORs) in nominal and orthogonal scan directions, often concatenated in pairs. For the very elongated EGS and $z \sim 1$ clusters we overweight maps scanning along the long axis, in order

---

[1] HCSS is a joint development by the *Herschel* Science Ground Segment Consortium, consisting of ESA, the NASA *Herschel* Science Center, and the HIFI, PACS and SPIRE consortia.
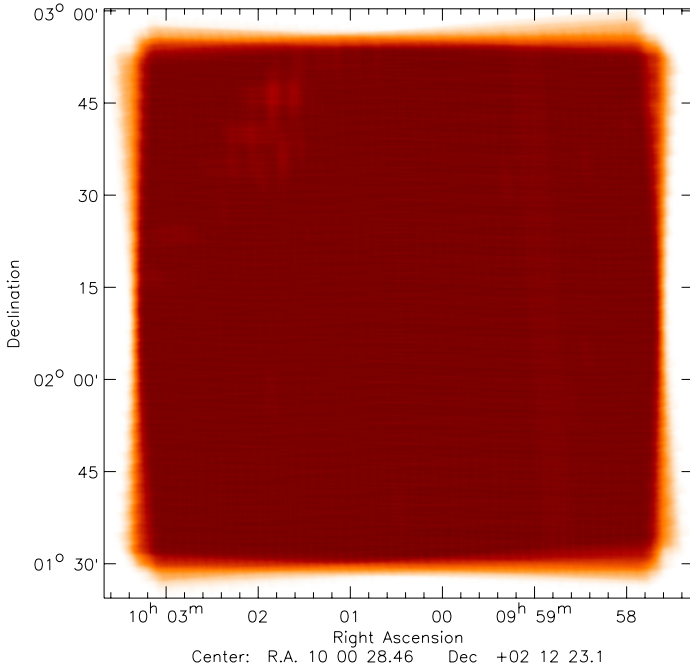
Fig. 2. Actual 160 μm coverage map of the COSMOS field. Spots of reduced coverage near the top left of the map are due to dropping of data because of "speed bumps" (see text).

to reduce overhead losses that are caused by the time spent in scan turnaround loops.

– Small cross-scan separations, specifically the size of one of the eight PACS "blue" detector array matrices (∼50″) or fractions 1/2 or 1/2.5 of it. Simple models demonstrate that for such a scan pattern homogeneous coverage maps are produced already from a single detector matrix, for any relative orientation of the scan direction and the inter-matrix gaps. By definition, this pattern also averages out sensitivity variations between detector matrices over most of the final map. If this redundant mapping scheme led to short execution times of a single scanmap over the field but deeper observations were needed, the scanmap was repeated within an AOR to reach a total execution time between one and a few hours.

– Often, many AOR pairs with a plausible execution time that does not exceed a few hours each, are still needed to achieve the required depth. Then, AOR positions may be dithered by a fraction of the cross-scan separation to further improve spatial redundancy, and the corner of the map where the scan is started may be varied.

The two square degree COSMOS field is a special case where the described observing strategy would lead to extremely long individual AORs. During one of the about two-month long *Herschel* visibility periods of COSMOS, the PACS arrays are always similarly oriented on this region of the sky, with a position angle of the long axis about 20 ± 10°. This permits an AOR setup in the efficient "homogeneous coverage" mode in array coordinates, keeping the individual AOR length below five hours but staying well matched to the roughly square nonrotated orientation of many COSMOS ancillary data sets. This is illustrated by the actual coverage map obtained with PACS (Fig. 2).

Table 2 provides the key parameters of the actual PACS AOR implementations for each field. No significant source variability is expected for the dust-dominated emission of almost all detected sources. For this reason no timing constraints needed to be

applied in the scheduling. For practical reasons, scheduling of all AORs of a field during a visibility period was aimed for, and was typically but not always achieved. For fields near the plane of the ecliptic (COSMOS), asteroid passages may introduce another time-dependent factor, as clearly demonstrated in mid-infrared detections during *Spitzer* observations of the COSMOS field (Sanders et al. 2007). The contrast between galaxies and asteroids is more favorable in the far-infrared. Still, bright asteroids would be detectable in individual maps if present but were not identified when taking differences of our individual COSMOS maps and a coadded map.

SPIRE maps for most of the PEP fields are obtained in coordinated observations by the HerMES key program (Oliver et al. 2011). For the two $z \sim 1$ clusters we implemented within PEP simple 10′ × 10′ "large" SPIRE scanmaps in nominal scan speed, spatially dithering between five concatenated independent repetitions.

4. Data analysis

4.1. Reduction of scanmap data and map creation

For scanning instruments with detectors that have a significant 1/f low frequency noise component, map creation usually follows one of two alternative routes. One is using full "inversion" algorithms as widely applied by the cosmic microwave background community and the other uses highpass filtering of the detector timelines and subsequent direct projection, frequently used for *Spitzer* MIPS 70 or 160 μm reductions. An algorithm of the first "inversion" type is available in the HCSS *Herschel* data processing in the form of an implementation and adaption to *Herschel* of a version of the MadMap code (Cantalupo et al. 2010). The alternative option that we adopt and describe in more detail below is using highpass filtering of the detector timelines and a direct "naive" mapmaking. This choice is made because for our particular case of deep field observations, MadMap presently does not reach the same point source sensitivity, and the preservation of diffuse emission is not important for our science case. As noted, the cross-linked design of the PEP observations, however, does permit the future application of such inversion codes.

Our reduction first proceeds on a per AOR level and is based on scanmap scripts for the PACS photometer pipeline (Wieprecht et al. 2009) in HCSS, with parameter settings and additions optimized for our science case. After retrieving PACS data and satellite pointing information we apply the first reduction steps to the time-ordered PACS data frames, identifying functional blocks in the data, flagging bad pixels, flagging any saturated data, converting detector signals from digital units to volts and the chopper position from digital units to physical angle.

After adding the instantaneous pointing obtained from the *Herschel* pointing product to the time-ordered data frames, we apply "recentering" corrections. These are derived by comparing PACS maps obtained in a separate first processing of partial datablocks to deep 24 μm catalogs with accurate astrometry. Deep radio catalogs can also be used successfully. The corrections are derived by stacking a PACS 100 μm or 70 μm map that is obtained typically from about 15 min of data, using for the stack the positions of 24 μm sources, and measuring the offset of the stacked PACS detection. The measured position offset is then corrected for this block of data in the original frames. The blocks used were typically restricted to one scan direction (all "odd" or "even" scanlegs of a map repetition, or

Table 2. AOR parameters used for the PEP fields.

Field	Nominal scan direction							Orthogonal scan direction						
	Leg ′	Step ″	N_L	Angle °		N_{Rep}	N_{AOR}	Leg ′	Step ″	N_L	Angle °		N_{Rep}	N_{AOR}
COSMOS	85	Hom	Sq	70	Arr	1	24	85	Hom	Sq	160	Arr	2	25
Lockman Hole XMM	24	50	30	0	Sky	2	10	24	50	30	90	Sky	2	10
EGS	67	50	13	4 0.5	Sky	2	13	10	50	81	130.5	Sky	2	8
ECDFS	30	50	37	0	Sky	2	8	30	50	37	90	Sky	2	8
GOODS-S 70/160	17	25	27	348.7	Sky	2	48	11	25	41	78.7	Sky	2	48
GOODS-S 100/160	17	25	27	348.7	Sky	2	54	11	25	41	78.7	Sky	2	54
GOODS-N	17	25	27	41	Sky	2	11	11	25	41	131	Sky	2	11
Cl0024+16	6	20	19	45	Arr	15	1	6	20	19	315	Arr	15	1
Abell 370	4	20	13	45	Arr	22	1	4	20	13	315	Arr	22	1
MS0451.6-0305	4	20	13	45	Arr	22	1	4	20	13	315	Arr	22	1
Abell 1689	4	20	13	45	Arr	18	3	4	20	13	315	Arr	18	3
RXJ1347.5-1145	4	20	13	45	Arr	22	1	4	20	13	315	Arr	22	1
MS1358.4+6245	4	20	13	45	Arr	22	1	4	20	13	315	Arr	22	1
Abell 1835	4	20	13	45	Arr	22	1	4	20	13	315	Arr	22	1
Abell 2218	4	20	13	45	Arr	14	3	4	20	13	315	Arr	14	3
Abell 2219	4	20	13	45	Arr	22	1	4	20	13	315	Arr	22	1
Abell 2390	4	20	13	45	Arr	22	1	4	20	13	315	Arr	22	1
RXJ0152.7-1357	10	25	13	45	Sky	6	3	5	25	25	135	Sky	2	3
MS1054.4-0321	10	25	13	0	Sky	6	3	5	25	25	90	Sky	2	3

Notes. For both the nominal and the orthogonal scan direction, the table lists the scan leg length, the cross-scan separation step, the number of scan legs, the scan angle and its reference system (Sky or Array), the number of scan repetitions within an AOR, and the number of independent AORs obtained with those settings. "Hom Sq" indicates that the cross-scan separation and number of scan legs are defined automatically by the AOT logic to produce a square map with "homogeneous" coverage.

subsets for the large COSMOS maps). By this procedure we correct for (1) the global offset pointing error of *Herschel*, which is around 2″ rms and thus non-negligible compared to PACS beam sizes; (2) differential pointing errors between different AORs that would lead to PSF smearing, in particular if AORs have been observed spread over long periods with different spacecraft orientations; (3) residual timing offsets between PACS data and pointing information that manifest themselves in small offsets between odd and even numbered scanlines; and (4) pointing drifts over ≳0.5 h timescales within an AOR. Overall this leads to subarcsecond astrometry and reduces unnecessary PSF smearing by pointing effects. As a verification of this approach, Fig. 3 compares the positions from a *blind* 100 μm catalog based on the final GOODS-N map with 24 μm positions.

Short glitches in the detector timelines caused by ionizing particle hits are flagged and interpolated with an HCSS implementation of the multiresolution median transform, developed by Starck & Murtagh (1998) to detect faint sources in ISOCAM data. The different signatures of real sources and glitches in the pixel timeline at medium scan speed are discriminated from each other by a multiscale transform. This procedure is known to produce false detections on bright point sources. This was no problem for our deep field data except for a few bright COSMOS sources for which we locally reduced the glitch-detection sensitivity.

The "1/f" noise of the PACS photometers, in fact roughly $\propto f^{-0.5}$ over the relevant frequencies, is removed by subtracting from each timeline the timeline filtered by a running box median filter of radius 15 samples (30″) at 70 μm or 100 μm and 26 samples (52″) at 160 μm. A mask is used to exclude sources from the median derivation. The mask is created by thresholding an S/N map produced from a smoothed coadded map that includes all AORs. Tests were done by adding simulated sources to the timelines before masking and before highpass filtering. These tests were made using the real timelines of the full Lockman Hole
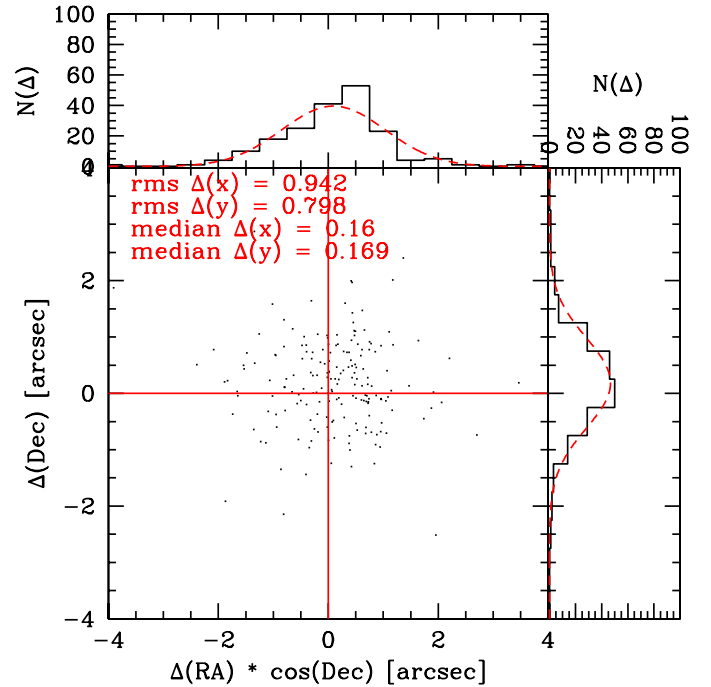

Fig. 3. Offsets of GOODS-N 100 μm sources detected at >5σ in a "blind" extraction, compared to the corresponding 24 μm positions of the MIPS catalog used by Magnelli et al. (2009). A global offset has already been subtracted when deriving the PACS map.

AOR set for the red filter, thus implicitly including all real sky structures. They indicate that the filtering modifies the fluxes by less than 5% for masked point sources and ~16% for very faint unmasked point sources. These results apply to "extragalactic deep field" skies that are composed of many point sources and

to our specific highpass filter setting. Extended sources need different filtering radii or reduction methods.

Flatfielding and flux calibration is done via the standard PACS pipeline calibration files. Because of the excellent in-flight stability of the photometer response, no use is made of the observations of the calibration sources internal to PACS that are obtained within each AOR. PEP science demonstration phase data were reduced using earlier versions of the responsivity calibration file and corrections derived on the stars γDra, αTau, and αCMA; they are within 5% of the currently valid Version 5 of the reponsivity calibration file that has been validated over a wider set of flux calibration stars and asteroids.

Before creating maps from the timelines we discard various unsuitable parts of the data:

1. Observations of the internal calibration sources and a short subsequent interval during which the signal re-stabilizes. SDP observations had an erroneously high scheduling rate of such calibration blocks.
2. Data taken during the turnaround loops between scans. The nominal pointing accuracy is not guaranteed during this phase, and highpass filtering effects on source flux are more severe if the telescope slows down strongly or even stops during a subtantial part of the filtering window.
3. Before a reduction of the star tracker operating temperature in *Herschel* operational day 320, "speed bumps" in the satellite movement occurred, when stars crossed irregularly behaving star tracker pixels. This led to an unknown mispointing. These events can be identified by comparing the two angular velocities obtained from (1) differentiation of the positions on sky reported in subsequent entries of the pointing product; and (2) the direct angular rate information in the pointing product.
4. Blue PACS bolometer data occasionally show fringes in the signal due to magnetic field interference that is heavily aliased into the timelines and final maps. Maps created separately for each individual scan line were visually inspected, and scans clearly affected by fringing excluded from final mapping.

Maps are obtained from the timelines for each AOR via the HCSS "photProject" projection algorithm, which is equivalent to a simplified version of the "drizzle" method (Fruchter & Hook 2002). Given the high data redundancy in the deep fields, PSF widths and noise correlation in the final map can be reduced by choosing smaller projection drops than the physical PACS pixel size. Drop sizes between 1/8 and 1/4 of the physical PACS pixel size were used, depending on redundancy of the individual maps for each field. Weights of the different detectors in the projection consider the inverse variance derived from the noise in the dataset itself.

Maps from each AOR were coadded into final maps, weighting the indivudal maps by the effective exposure of each pixel. The final error map was computed as the standard deviation of the weighted mean. PSF fitting using the methods described in Sect. 4.2 assumes errors that are uncorrelated between neighboring pixels. In practice, correlations exist due to projection and due to to the correlations that are caused by residual 1/f noise in the filtered timelines, in particular along the scan direction. We have verified that, because of the high redundancy of the data, these correlations are close to uniform across the final GOODS-N map, with less than 2% variation in the correction factor that is derived below. Thus from PSF shape and correlation information we derived a mean correlation correction factor which was then accounted for in the errors on the extracted
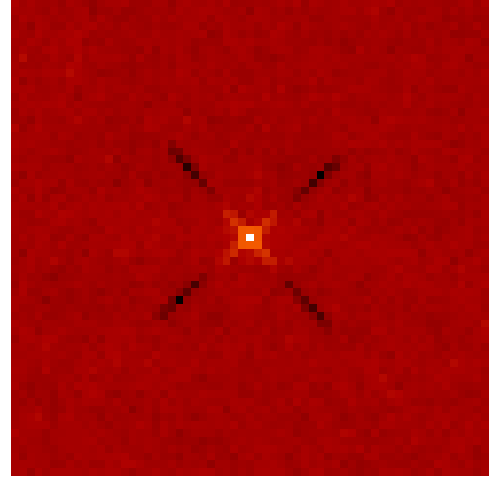

Fig. 4. Correlation map extracted from GOODS-N 100 μm data, reflecting correlations induced by map projection and – in scan direction – by residual low-frequency noise and highpass filtering. Correlations are shown as a function of relative Δx, Δy pixel positions, represented here with respect to the central pixel.

fluxes. To construct a correlation map, we first collect series of paired pixel values with same relative pixel coordinate offsets i, j. We take values Δf defined as the deviation in flux of a pixel in an individual AOR map from the corresponding pixel in the final map. This is a deviation from the mean with expectation value 0. These values are taken for a large number of pairs in different positions in each AOR map and from different AORs. For each pixel-pair series $\Delta f_{1,2}$, which corresponds to a specific i, j pixel offset, a correlation coefficient is calculated:

$$\rho(i, j) = \frac{\sum \Delta f_1 \Delta f_2}{\sqrt{\sum (\Delta f_1)^2} \sqrt{\sum (\Delta f_2)^2}}. \tag{1}$$

The correlation coefficients are stored as a map and written to the i, j position relative to the central pixel. Figure 4 shows an example correlation map. Normal error propagation for a weighted sum $g(x_1..x_n) = \sum_{k=1}^{n} a_k \cdot x_k$, where the error are σ_k and correlation coefficients $\rho(k, l)$ is

$$\sigma_g^2 = \sum_{k,l=1}^{n} a_k \sigma_k \, a_l \sigma_l \, \rho(k, l). \tag{2}$$

Given a PSF stamp with pixel values P_k and a correlation between every two pixels $\rho(i, j)$ known from their relative position, the correlation correction factor to the derived errors is:

$$f^2 = \frac{\sum_k P_k^2}{\sum_{i,j} P_i P_j \rho(i, j)}. \tag{3}$$

Here, f is the ratio of the propagated error without correlations and the error calculated with the correlation terms. This assumes a near uniform error map on the scale of a PSF. For the typical pixel sizes (2″ and 3″ at 100 μm and 160 μm) and projection parameters used in the PEP SDP reductions, the corrections are about $f \approx 1.4$ for the 70 μm and 100 μm maps and $f \approx 1.6$ for the 160 μm maps.

Before availability of version 6 of the ArrayInstrument calfile that contains the spatial transformation from PACS focal plane to sky, 160 μm data showed a ≈ 1″ spatial offset from 70 μm or 100 μm data. We corrected for this ad hoc in the 160 μm map fits headers, using offsets derived from a comparison of preliminary catalogs in the two bands.
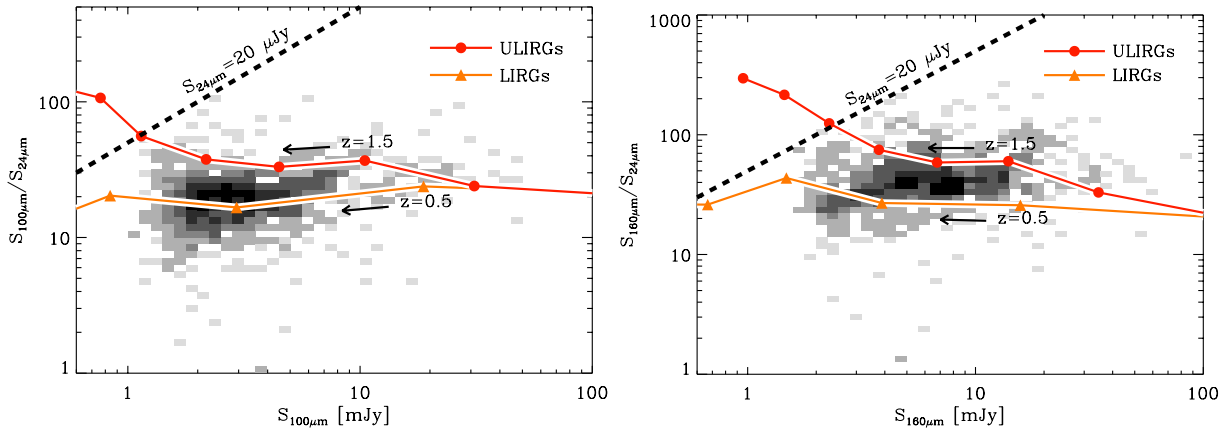
Fig. 5. *(Left)* PACS 100 μm to MIPS 24 μm flux density ratio as a function of the PACS 100 μm prior catalog flux density. Shaded grey regions show the space density distribution of galaxies observed in the GOODS-S field. In that field, the MIPS 24 μm and PACS 100 μm catalogs reach at 3-σ limit of 20 μJy and 1.2 mJy, respectively. Red dots and orange triangles present the evolution with redshift of the PACS-to-MIPS flux density ratio of ultra-luminous (ULIRGs) and luminous (LIRGs) infrared galaxies, respectively, predicted using the Chary & Elbaz (2001) library. Each symbol corresponds to a given redshift, in intervals of $\Delta z = 0.5$. On each track, we indicate on one point its corresponding redshift, as well as as the path followed for increasing redshifts. The dashed black line represents the limit of the parameter space reachable using the MIPS 24 μm catalog available in this field; all the PACS 100 μm sources below this line will have a MIPS 24 μm counterpart in this catalog. *(Right)* PACS 160 μm to MIPS 24 μm flux density ratio as function of the PACS 160 μm flux density. Symbols and lines are the same as in the *left* panel.

4.2. Catalog creation

We have extracted source catalogs using point source fitting routines outside HCSS. We used both blind extraction via the Starfinder PSF-fitting code (Diolaiti et al. 2000) and a guided extraction using 24 μm source priors, following the method described in Magnelli et al. (2009). We fitted with point spread functions extracted from the maps. Since these observed PSFs are limited in radius, we used point spread functions obtained on Vesta[2] for aperture corrections. To match the observations, these were rotated to match the satellite position angle for each observation of a field, coadded and slightly convolved with a Gaussian to match the actual *FWHM* of the combined map. For our reduction methods and projection into 2″ map pixels at 70 and 100 μm and 3″ at 160 μm, we have PSF *FWHM* for the 70, 100, and 160 μm maps of 6.46″, 7.39 ± 0.10″, and 11.29 ± 0.1″. The *FWHM* values are from Gaussian fits to the core of the observed PSF. For the 100 and 160 μm widths, we quote the error of the mean of measurements from five different fields.

All PEP blank fields benefit from extensive multiwavelength coverage that allows guided extraction based on source positions at shorter wavelengths, where the depth and resolution of the observations are higher. This approach resolves most of the blending issues encountered in dense fields and allows straightforward multiwavelength association (Magnelli et al. 2009, 2011; Roseboom et al. 2010). However, to use this powerful method, prior source catalogs have to contain all the sources in the PACS images. Deep MIPS 24 μm observations, available for all our blank fields, should fulfill this criterion since they have higher resolution and are deeper than our current PACS observations. Moreover, since the 24 μm emission is strongly correlated with the far-infrared emission, those catalogs will not contain a large excess of sources without far-infrared counterparts. This largely avoids deblending far-infrared sources into several unrealistic counterparts, as could happen when using an optical prior catalog with very high source density. Figure 5 illustrates the validity of the MIPS 24 μm observations as PACS prior source positions.

At 100 μm, models and observations predict typical PACS-to-MIPS flux ratios in the range 5–50. A MIPS 24 μm

catalog 50 times deeper than the PACS observations is thus suited to performing guided source extraction. This is illustrated, for GOODS-S, in the *left* panel of Fig. 5, where the observed PACS population lies well below the boundary of the parameter space reachable by the MIPS 24 μm catalog. In all our blank fields, deep MIPS 24 μm catalogs fulfill this criterion (i.e., GOODS-S/N, COSMOS, LH, ECDFS, EGS, etc.).

At 160 μm, models and observations have typical PACS-to-MIPS flux ratios in the range 15–150. In all but one field, the deep MIPS 24 μm observations are at least 150 times deeper than our PACS observations; thus, they can be used as prior source positions. In GOODS-S, the deepest MIPS 24 μm observations are only 100 times deeper than our PACS observations. This limitation can be observed in the *right* panel of Fig. 5 as a slight truncation, at faint 160 μm flux density, of the high-end of the dispersion of the PACS-to-MIPS flux ratio. This truncation will introduce, at faint flux density, incompleteness into our prior catalog. However, we also observe that even at this faint 160 μm flux density, the bulk of the population has a PACS-to-MIPS flux ratio of ~60. The incompleteness introduced by the lack of MIPS 24 μm priors should thus be low or at least lower than the incompleteness introduced by source extraction methods at such a low S/N. This was checked by comparing the GOODS-S 160 μm catalog obtained using blind source extraction with the one obtained using guided source extraction: we find no significant difference, at faint 160 μm flux densities, in the number of sources in those two catalogs. In line with these findings, Magdis et al. (in prep) find very low fractions of 24 μm undetected sources in very deep data from the GOODS-*Herschel* key program, <2% for ratios of detection limits S(100)/S(24) > 43 and <1% for S(160)/S(24) > 130.

Therefore, for all fields with deep MIPS 24 μm observations, we also extract source catalogs with a PSF-fitting method using 24 μm source positions as priors and following the method described in Magnelli et al. (2009). We used the same PSFs and aperture corrections as for the blind source extraction. Blind and prior catalogs were compared to verify the consistency between those two methods.

Completeness, fraction of spurious sources, and flux reliability were estimated by running Monte Carlo simulations.

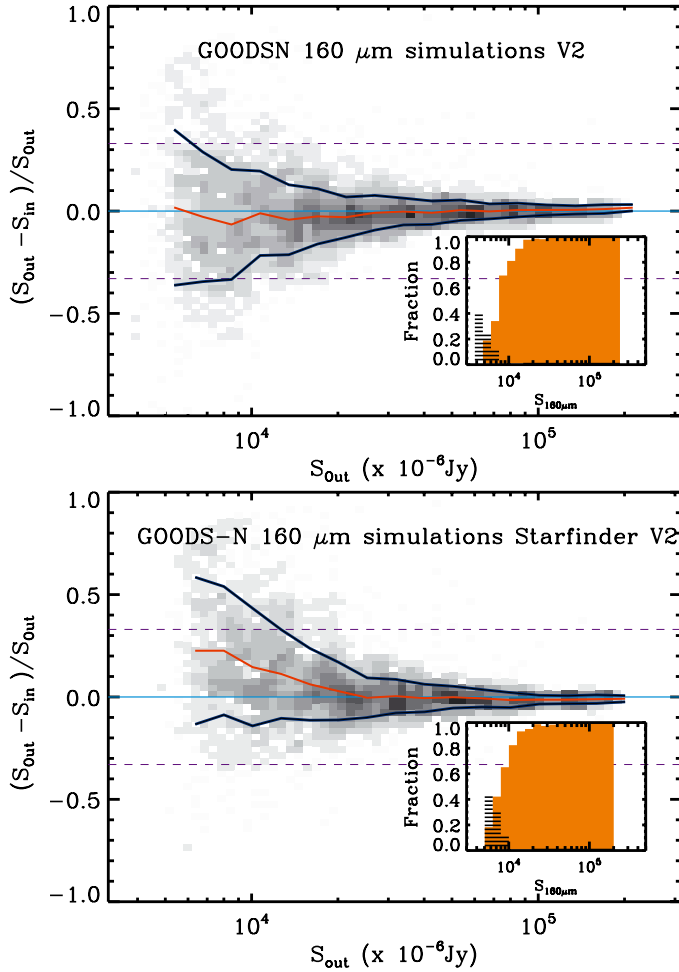[2] Accompanying PACS ICC document PICC-ME-TN-033 version 0.3.

Fig. 7. Noise estimate from randomly placing apertures on the GOODS-N 160 μm residual map.

3σ (Image). The systematic flux boosting in the blind extraction is corrected in the final blind catalog on the basis of these simulations. Given that, input and output fluxes are consistent with each other within a few percent, testifying that PACS fluxes are reliably extracted and retrieved by the adopted source extraction methods.

Noise was estimated by extracting fluxes through 10 000 apertures randomly positioned on residual maps. Figure 7 shows the distribution of the extracted fluxes, peaking around zero, as expected for a well subtracted background, and showing a Gaussian profile.

5. Science demonstration phase data

Figures 8 and 9 show the 100 μm and 160 μm maps of the GOODS-N and Abell 2218 fields as obtained during the *Herschel* science demonstration phase. A conservative threshold of 90% completeness is reached for the blind catalogs near 7 mJy and 15 mJy for 100 μm and 160 μm in the main parts of both GOODS-N and A2218. Above that level, the blind catalogs contain 153 and 126 sources for GOODS-N and 49 and 47 for Abell 2218, respectively. At the time of these observations, the *Herschel* scan maps were still exhibiting larger turnaround overheads than implemented later, and the PACS scanmap AOR had an unnecessarily high rate of internal calibrations. Both these factors do not significantly affect the maps, which are based on highpass-filtered reductions. With the exception of the overheads, these observations are representative of the results achievable in later mission periods during the observing times listed in Table 1, which reflect the later reduced overheads.

Figure 10 compares 100 μm fluxes for the GOODS-N field between the blind (starfinder) extraction and extraction based on 24 μm priors. The blind detections have here been associated a posteriori to 24 μm sources, using a modification of the maximum likelihood method of Ciliegi et al. (2001). The agreement is satisfactory with no systematic flux differences. Deviations occur at low fluxes where either catalog is incomplete and for few outliers where algorithms disagree in splitting a peak into two sources compared to one.

Figure 11 shows a "color-magnitude" diagram for 160 μm detected sources in GOODS-N. As expected, there is a tendency for higher redshift sources to be redder in the 160/100 μm flux ratio, with considerable scatter due to measurement error

Fig. 6. Results of artificial source addition experiments for the GOODS-N 160 μm extractions. *Top*: prior extraction, *Bottom*: blind extraction. The red lines represent the average photometric accuracy, blue lines set the standard deviation observed in each flux bin (after 3σ clipping). The systematic boosting in the blind extraction is corrected in the final blind catalog. The orange histogram represents the detection rate (or completeness) computed on the artificial injected sources, while black histograms denote the fraction of spurious sources as a function of output flux.

Up to 10 000 artificial sources were added to PACS science maps, and then extracted with the same techniques and configurations adopted for real source extraction. In order to avoid crowding, many such frames were created, each including a limited number of artificial sources. The number of frames and the number of sources added in each one depend on the size of the field under analysis and range between 20 and 500 sources (GOODS fields or COSMOS) per frame, repeated up to reaching the total of 10 000. These synthetic sources cover a wide range in flux, extending down to 0.5σ (with σ the measured rms noise in the PACS maps). The flux distribution follows the detected number counts, extrapolated to a fainter level by means of the most successful fitting backward evolutionary model predictions (see Berta et al. 2011). Sources are modeled with the Vesta PSF, manipulated as described above.

Figure 6 shows an example of results in the GOODS-N field at 160 μm. Completeness is defined here as the fraction of sources that have been detected with a photometric accuracy of at least 50% (Papovich et al. 2004). Spurious sources are defined as those extracted above 3σ with an input flux lower than
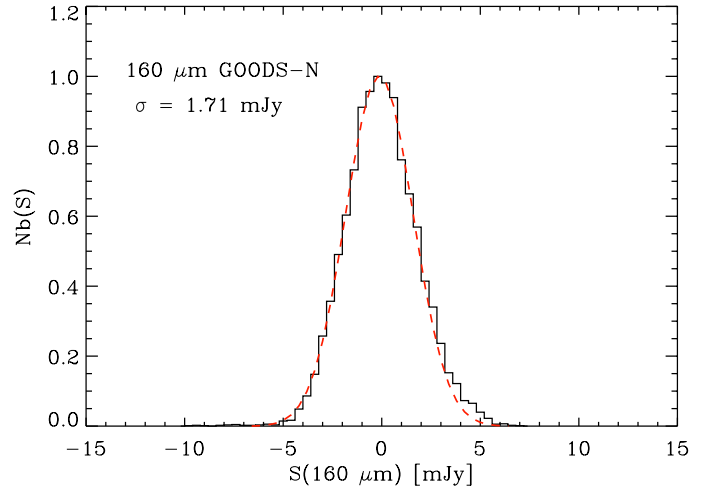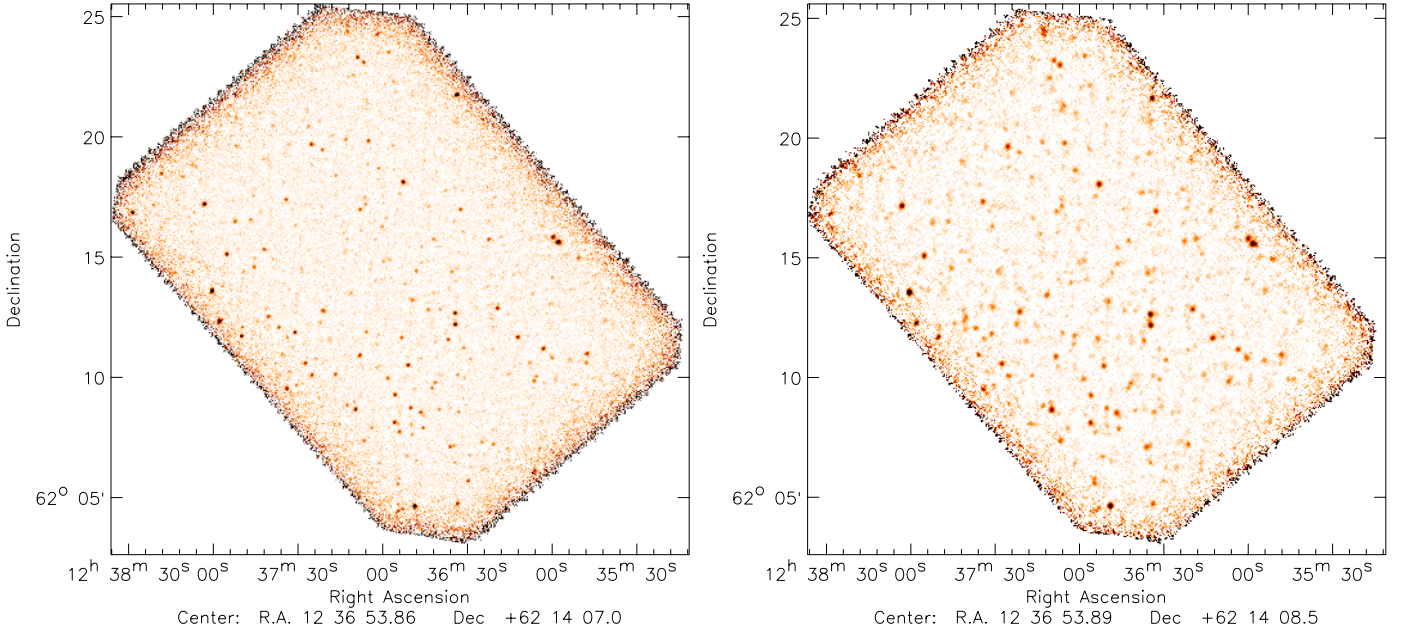
Fig. 8. Science demonstration phase maps of the GOODS-N field. *Left*: 100 μm. *Right*: 160 μm.
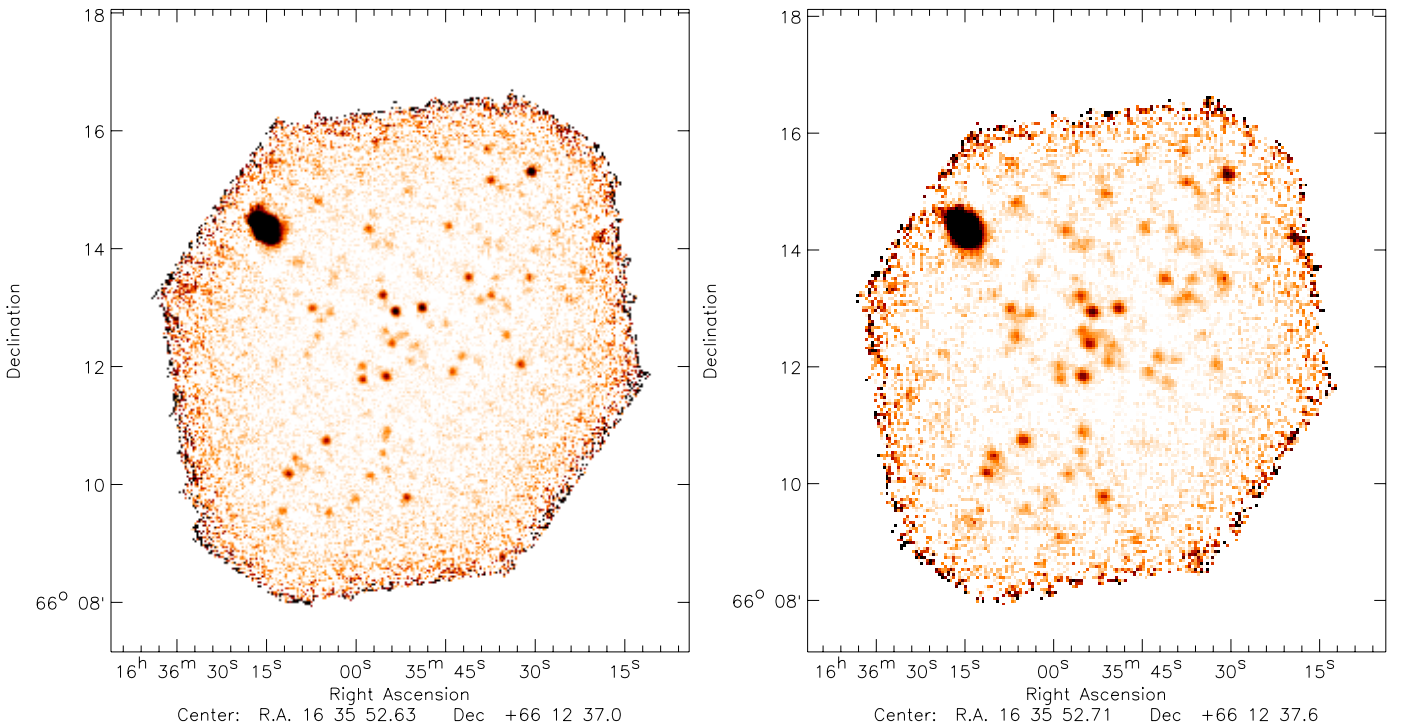

Fig. 9. Science demonstration phase maps of the Abell 2218 lensing cluster field. *Left*: 100 μm. *Right*: 160 μm.

and variation in the population. A detailed discussion of colors and SEDs is outside the scope of this work, but see also Elbaz et al. (2010), Magnelli et al. (2010), Hwang et al. (2010) and Dannerbauer et al. (2010) for first results on GOODS-N SEDs.

Figure 12 illustrates the potential of PEP to reach normal star-forming galaxies up to redshifts $z \sim 2$. The GOODS-N science demonstration phase data reach at $z \sim 2$ infrared luminosities of 10^{12} $L_{\odot}$ (star formation rates about 100 solar masses per year). The GOODS-N SDP observation thus reaches

the star formation "main sequence" for massive galaxies at that redshift (Daddi et al. 2007a). The GOODS-S data go deeper by a factor ≥ 2, and the COSMOS data provide the precious statistics at higher luminosities.

As an example of the PEP/PACS performance for deep surveys, the >90% completeness blind catalogs of the GOODSN and Abell 2218 SDP data will be released on the PEP website[3].
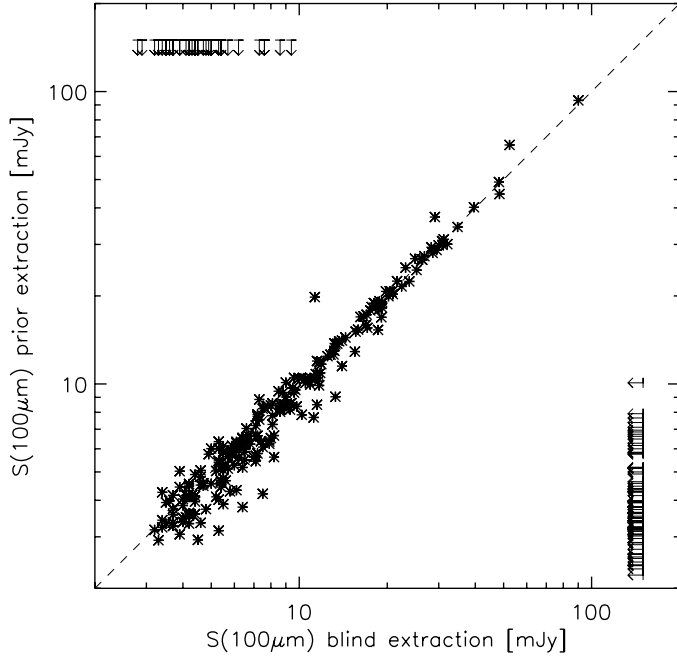
---

[3] http://www.mpe.mpg.de/ir/Research/PEP/index.php

Fig. 10. Comparison of blindly extracted and prior extracted 100 μm fluxes for the GOODS-N field.
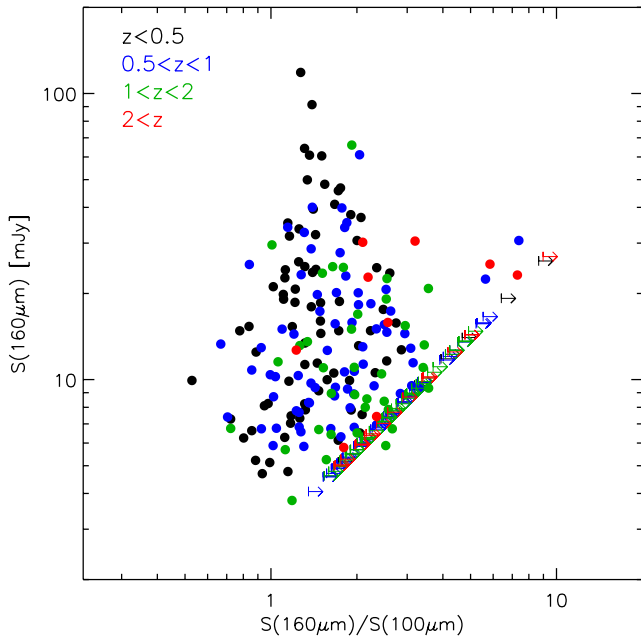

Fig. 11. Color–magnitude diagram for 160 μm detected sources in the GOODS-N field.

6. Overview of first science results of the PEP survey

6.1. The cosmic infrared background

One of the most imminent tasks of a large far-infrared space telescope is to resolve a large fraction of the cosmic infrared background into its constituent galaxies. The CIB peaks at roughly 150 μm (e.g., Dole et al. 2006), making *Herschel*/PACS excellently suited to characterizing the sources of its bulk energy output. Berta et al. (2010) used SDP observations of GOODS-N to derive 100 and 160 μm number counts down to 3.0 and 5.7 mJy, respectively. Altieri et al. (2010) used strong lensing by the
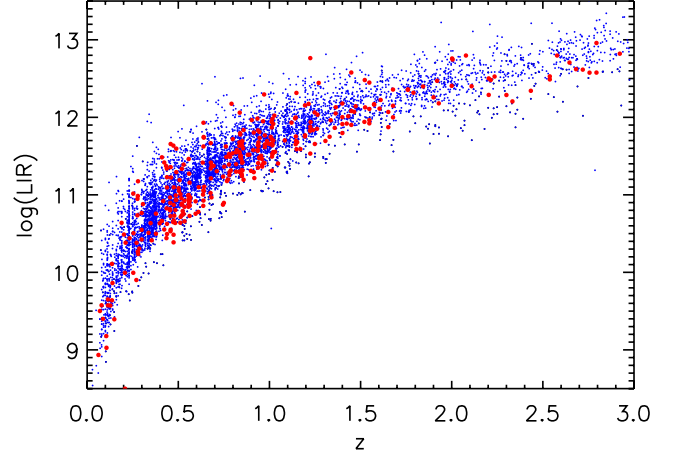

Fig. 12. Red: Total infrared luminosity of GOODS-N sources detected above 3σ in the PEP SDP data. Blue: Sources from the GOODS-S and COSMOS data illustrate the potential of the full PEP survey.

massive cluster Abell 2218 to push this limit down to 1 and 2 mJy, deeper by a factor ~3 for both wavelengths. Berta et al. (2011) use a complement of PEP blank field observations including the deep GOODS-S observations to reach a depth similar to Altieri et al. but with the larger statistics provided by the blank field observations. They also add 70 μm counts overall reaching 1.1, 1.2, and 2.4 mJy in the three PACS bands. To this depth, 58% (74%) of the COBE CIB as quoted by Dole et al. (2006) is resolved into individually detected sources at 100 (160 μm). These fractions reach 65% (89%) when including a P(D) analysis.

It is important to note that the direct COBE/DIRBE measurements have considerable uncertainties due to the difficulty of foreground subtraction. Similar to other wavelengths such as the <10 keV X-rays (e.g., Brandt & Hasinger 2006) we are reaching the point where the lower limits to the cosmic background that are provided by the integral of the resolved *Herschel* measurements are more constraining than the direct measurements. Quoting "resolved fractions" in reference to COBE thus starts to become problematic.

Because of the excellent multiwavelength coverage of the PEP fields, spectroscopic or photometric redshifts can be assigned to the detected sources, allowing us to determine the redshifts at which the CIB originates. To the depth reached by Berta et al. (2011), half of the resolved CIB originates at $z > 0.58$, 0.67, 0.73 for wavelengths of 70, 100, and 160 μm, respectively. These redshifts are mild lower limits because they exclude faint sources that are not individually detected by *Herschel*, and naturally increase with wavelength, reflecting the dominant contributions by the far-infrared SED peak of increasingly distant objects.

Comparing the PEP counts and redshift distributions to backward evolutionary models derived from pre-*Herschel* data, Berta et al. (2011) find reasonable agreement for several models with the total counts but more significant mismatches to the observed redshift distributions. Clearly, models have to be modified in order to provide a satisfactory representation of the most recent data including *Herschel*.

The PEP GOODS-N SDP data have been used to derive first direct far-infrared based luminosity functions up to $z \sim 2$–3 (Gruppioni et al. 2010). Strong evolution of the comoving infrared luminosity density (proportional to the star formation rate density) is found, increasing with redshift as $(1 + z)^{3.8\pm0.3}$ up to

$z \sim 1$. Global classification of the SEDs assigns to most objects either a starburst-like SED or an SED that suggests a modest AGN contribution.

6.2. "Calorimetric" far-infrared star formation rates and star formation indicators

Star formation rates are one of the key measurables in galaxy evolution studies. "Calorimetric" rest-frame, far-infrared measurements are the method of choice for massive and in particular dusty galaxies, but have been out of reach for typical high-z galaxies in the pre-*Herschel* situation. Typically, star formation rates were measured from the rest-frame ultraviolet, mid-infrared, submm/radio, or a combination of those methods. All of them require certain assumptions. Extracting a star formation rate from the rest frame ultraviolet continuum involves breaking the degeneracies between the star formation history and obscuration, and involves assumptions about the dust extinction law and/or geometry of the obscuring dust. Extrapolation from the mid-infrared or submm/radio requires adopting SED templates or assumptions that were derived locally but insufficiently tested at high redshift.

Nordon et al. (2010) focused on massive $z \sim 2$ normal starforming galaxies that are currently the subject of intense study towards the role of secular and merging processes in their evolution (e.g., Förster Schreiber et al. 2009). They found ultraviolet-based star formation rates reasonably confirmed. At the rest frame optical bright end of these bright star-forming galaxies, UV SFRs overpredict the calorimetric measurement by a factor 2 only. In contrast, a significant overprediction by a factor ~4–7.5 was found when extrapolating from the 24 μm flux assuming that the local Universe Chary & Elbaz (2001) templates apply *for the given mid-IR luminosity*. This is in line with the encompassing SED studies of Elbaz et al. (2010) and Hwang et al. (2010) that, combining PEP and HerMES as well as local Akari data, found that this overprediction by 24 μm extrapolation sets in at $z \sim 1.5$, and that the FIR SED temperatures of high z galaxies are modestly colder than their local equivalents of similar total infrared luminosity.

There are two ways of looking at these results. Comparing at same total IR luminosity local galaxies with $z \sim 2$ galaxies, the $z \sim 2$ "overprediction" when extrapolating from the mid-IR could either be due to an enhanced ratio of the PAH complex to the FIR peak, or due to a boosting of the mid-infrared emission via the continuum of a possibly obscured AGN (see also Papovich et al. 2007; Daddi et al. 2007b). While most likely both factors are at work to some level, the fact that the 24 μm overprediction sets in at $z \sim 1.5$, as well as Spitzer spectroscopy of mid-IR galaxies at these redshifts (Murphy et al. 2009; Fadda et al. 2010), argues for the dominant role of stronger PAH. This is established by Nordon et al. (2011) who show that $z \sim 2$ GOODS-S galaxies with large 24 μm/FIR ratios indeed have PAH-dominated spectra in the Fadda et al. (2010) sample.

It is important to put this into the perspective of other properties of $L_{IR} \sim 10^{12} \, L_{\odot}$ local and $z \sim 2$ galaxies. Locally, such an object is a classical interacting or merging "ultraluminous infrared galaxy" (ULIRG, Sanders & Mirabel 1996) with star formation concentrated in a few hundred parsec sized region. Such star formation rates are well above the local "main sequence" (Brinchmann et al. 2004). At $z \sim 2$, objects with the same star formation rates can be on the main sequence (Daddi et al. 2007a) and are often not interacting/merging but massive, turbulent disks with star formation spread out over several kpc (e.g., Genzel et al. 2008; Shapiro et al. 2008;

Förster Schreiber et al. 2009). It is therefore not surprising that SED templates calibrated on local compact mergers fail to reproduce the more extended star formation at $z \sim 2$. The locally defined connotations of the "ULIRG" term, beyond its basic definition by IR luminosity, obviously do not apply automatically at high redshift.

Rodighiero et al. (2010) use the direct *Herschel* far-infrared star formation rates in the PEP GOODS-N field to characterize the evolution of the specific star formation rate (SSFR)/mass relation up to $z \sim 2$. They find a steepening from an almost flat local relation to a slope of –0.5 at $z \sim 2$.

Concerning the most highly star-forming high-redshift objects, Magnelli et al. (2010) combine the GOODS-N and Abell 2218 PACS data with submm surveys. They use PACS to sample the Wien side of the far-infrared SED of submm galaxies and optically faint radio galaxies with accurately known redshifts. The directly measured dust temperatures and infrared luminosities are in good agreement with estimates that are based on radio and submm data and are adopting the local universe radio/far-infrared correlation (see also the dedicated PEP/HerMES test of the high-z radio/far-infrared correlation by Ivison et al. (2010). This confirmation of huge O(1000 $M_{\odot}$ yr^{-1}) star formation rates for SMGs supports the predominantly merger nature of SMGs, since such star formation rates are very hard to sustain with secular processes (e.g., Davé et al. 2010).

6.3. The role of environment

PEP data cover a wide range of environments. As first steps, Magliocchetti et al. (2011) derive correlation functions and co-moving correlation lengths at $z \sim 1$ and 2 from the GOODS-S data, which also provide evidence for most infrared bright $z \sim 2$ galaxies in this field residing in a filamentary structure. At $z \sim 1$, Popesso et al. (2011) observe a reversal of the local star formation rate - density relation that is linked to the presence of AGN hosts that in turn favor high stellar masses, dense regions, and high star formation rates.

6.4. Studies of individual galaxy populations

Dannerbauer et al. (2010) use the $\lesssim 10''$ beam PEP maps to verify the identifications of (sub)millimeter galaxies and test the potential of PACS colors and mid-infrared to radio photometric redshifts for these objects. Santini et al. (2010) use the *Herschel* points to break the degeneracy between dust temperature and dust mass that is inherent in submm-only data, and derive high dust masses for a sample of submillimeter galaxies. Comparison of these high dust masses with the relatively low gas-phase metallicities either implies incompletely understood dust properties or a layered structure that combines low-metallicity visible outer regions with a highly obscured interior.

Magdis et al. (2010) used a stacked detection of $z \sim 3$ Lyman break galaxies to constrain their far-infrared properties. Similar to the SMG/OFRG study of Magnelli et al. (2010), this work highlights the selection effects in the luminosity / dust temperature plane that are imposed by groundbased submm detection. Bongiovanni et al. (2010) study Lyman α emitters in the GOODS-N field. PACS detections of part of these galaxies are evidence of overlap with the dusty high-redshift galaxy population.

6.5. AGN-host coevolution: two modes?

Within the complex task of disentangling the coevolution of AGN and their host galaxies, and the role of AGN feedback, rest-frame far-infrared observations provide a unique opportunity to determine host star formation rates. This rests on the assumption that the host dominates the AGN in the rest frame far-infrared. This assumption is motivated by determinations of the intrinsic SED of the AGN proper, which is found to drop towards the far-infrared (e.g., Netzer et al. 2007; Mullaney et al. 2011). Compared to previous attempts from the submm (e.g., Lutz et al. 2010) and Spitzer (e.g., Mullaney et al. 2010), *Herschel* performance provides a big step forward. Shao et al. (2010) use the PEP GOODS-N observations and the *Chandra* Deep Field North to map out the host star formation of AGN of different redshifts and AGN luminosities. The host far-infrared luminosity of AGN with $L_{2-10\,\mathrm{keV}} \approx 10^{43}$ erg s^{-1} increases with redshift by an order of magnitude from $z = 0$ to $z \sim 1$, similar to the increase with redshift in the star formation rate of inactive massive galaxies. In contrast, there is little dependence of far-infrared luminosity on AGN luminosity, for $L_{2-10\,\mathrm{keV}} \lesssim 10^{44}$ erg s^{-1} AGN at $z \gtrsim 1$. In conjunction with properties of local and luminous high-z AGN, this suggests an interplay between two paths of AGN/host co-evolution. A correlation of AGN luminosity and host star formation for luminous AGN reflects an evolutionary connection, likely via merging. For lower AGN luminosities, star formation is similar to that in nonactive massive galaxies and shows little dependence on AGN luminosity. The level of this secular, not merger-driven star formation increasingly dominates the correlation at increasing redshift.

7. Conclusions

Deep *Herschel* far-infrared surveys are a powerful new tool for studying galaxy evolution and for unraveling the constituents of the cosmic infrared background. We have described here the motivation, field selection, observing strategy, and data analysis for the PEP guaranteed time survey. The science demonstration phase data of GOODS-N and Abell 2218 are discussed to illustrate the performance of *Herschel*-PACS for this science. The wide range of initial science results from the PEP data is briefly reviewed.

References

Altieri, B., Berta, S., Lutz, D., et al. 2010, A&A, 518, L17
Aussel, H., Cesarsky, C. J., Elbaz, D., & Starck, J. L. 1999, A&A, 342, 313
Berta, S., Magnelli, B., Lutz, D., et al. 2010, A&A, 518, L30
Berta, S., Magnelli, B., Nordon, R., et al. 2011, A&A, 532, A49
Bongiovanni, A., Oteo, I., Cepa, J., et al. 2010, A&A, 519, L4
Brandt, W. N., & Hasinger, G. 2006, ARA&A, 43, 827
Brinchmann, J., Charlot, S., White, S. D. M., et al. 2004, MNRAS, 351, 1151
Cantalupo, C. M., Borill, J. D., Jaffe, A. H., Kisner, T. S., & Stompor, R. 2010, ApJS, 187, 212
Chary, R., & Elbaz, D. 2001, ApJ, 556, 562
Ciliegi, P., Gruppioni, C., McMahon, R., & Rowan-Robinson, M. 2001, Ap&SS, 276, 957
Daddi, E., Dickinson, M., Morrison, G., et al. 2007a, ApJ, 670, 156
Daddi, E., Alexander, D. M., Dickinson, M., et al. 2007b, ApJ, 670, 173
Dannerbauer, H., Daddi, E., Morrison, G. E., et al. 2010, ApJ, 720, L144
Davé, R., Finlator, K., Oppenheimer, B. D., et al. 2010, MNRAS, 404, 1355
Davis, M., Guhathakurta, P., Konidaris, N. P. et al. 2007, ApJ, 660, L1
Diolaiti, E., Bendinelli, O., Bonaccini, D., et al. 2000, A&AS, 147, 335
Dole, H., Rieke, G. H., Lagache, G., et al. 2004, ApJS, 154, 93
Dole, H., Lagache, G., Puget, J.-L., et al. 2006, A&A, 451, 417
Eales, S., Dunne, L., Clements, D., et al. 2010, PASP, 122, 499
Ebeling, H., Jones, L. R., Perlman, E., et al. 2000, ApJ, 543, 133
Egami, E., Rex, M., Rawle, T. D., et al. 2010, A&A, 518, L12
Elbaz, D., Hwang, H. S., Magnelli, B., et al. 2010, A&A, 518, L29
Elbaz, D., Dickinson, M., Hwang, H. S., et al. 2011, A&A, submitted [arXiv:1105.2537]
Fadda, D., Yan, L., Lagache, G., et al. 2010, ApJ, 719, 425
Förster Schreiber, N. M., Genzel, R., Bouché, N., et al. 2009, ApJ, 706, 1364
Fruchter, A. S., & Hook, R. N. 2002, PASP, 114, 144
Genzel, R., & Cesarsky, C. 2000, ARA&A, 38, 761
Genzel, R., Burkert, A., Bouché, N., et al. 2008, ApJ, 687, 59
Griffin, M., Abergel, A., Abreu, A., et al. 2010, A&A, 518, L3
Gruppioni, C., Pozzi, F., Andreani, P., et al. 2010, A&A, 518, L27
Hasinger, G., Altieri, B., Arnaud, M., et al. 2001, A&A, 365, L45
Hauser, M. G., Arendt, R. G., Kelsall, T., et al. 1998, ApJ, 508, 25
Hopkins, A. M., & Beacom, J. F. 2006, ApJ, 651, 142
Hughes, D. H., Serjeant, S., Dunlop, J., et al. 1998, Nature, 393, 241
Hwang, H. S., Elbaz, D., Magdis, G., et al. 2010, MNRAS, 409, 75
Ivison, R. J., Magnelli, B., Ibar, E., et al. 2010, A&A, 518, L31
Kiss, Cs., Ábrahám, P., Klaas, U., et al. 2001, A&A, 399, 177
Le Floc'h, E., Papovich, C., Dole, H., et al. 2005, AJ, 632, 169
Lehmer, B. D., Brandt, W. N., Alexander, D. M., et al. 2005, ApJS, 161, 21
Lilly, S. J., Le Fevre, O., Hammer, F., & Crampton, D. 1996, ApJ, 460, L1
Lutz, D., Mainieri, V., Rafferty, D., et al. 2010, ApJ, 712, 1287
Madau, P., Ferguson, H. C., Dickinson, M. E., et al. 1996, MNRAS, 283, 1388
Magdis, G., Elbaz, D., Hwang, H. S., et al. 2010, ApJ, 720, L185
Magliocchetti, M., Santini, P., Rodighiero, P., et al. 2011, MNRAS, in press [arXiv:1105.4093]
Magnelli, B., Elbaz, D., Chary, R. R., et al. 2009, A&A, 496, 57
Magnelli, B., Lutz, D., Berta, S., et al. 2010, A&A, 518, L28
Magnelli, B., Elbaz, D., Chary, R. R., et al. 2011, A&A, 528, A35
Mullaney, J. R., Alexander, D. M., Huynh, M., Goulding, A., & Frayer, D. 2010, MNRAS, 401, 995
Mullaney, J. R., Alexander, D. M., Goulding, A. D., & Hickox, R. C. 2011, MNRAS, 414, 1082
Murphy, E. J., Chary, R.-R., Alexander, D. M., et al. 2009, ApJ, 698, 1380
Netzer, H., Lutz, D., Schweitzer, M., et al. 2007, ApJ, 666, 806
Nordon, R., Lutz, D., Shao, L., et al. 2010, A&A, 518, L24
Nordon, R., Lutz, D., Berta, S., et al. 2011, ApJ, submitted [arXiv:1106.1186]
Oliver, S., et al. 2011, MNRAS, submitted
Papovich, C., Dole, H., Egami, E., et al. 2004, ApJS, 154, 70
Papovich, C., Rudnick, G., Le Floc'h, e., et al. 2007, ApJ, 668, 45
Pilbratt, G., Riedinger, J. R., Passvogel, T. et al. 2010, A&A, 518, L1
Poglitsch, A., Waelkens, C., Geis, N., et al. 2010, A&A, 518, L2
Popesso, P., Rodighiero, G., Saintonge, A., et al. 2011, A&A, in press [arXiv:1104.1094]
Puget, J.-L., Abergel, A., Bernard, J.-P., et al. 1996, A&A, 308, L5
Rodighiero, G., Cimatti, A., Gruppioni, C., et al. 2010, A&A, 518, L25
Roseboom, I. G., Oliver, S., Kunz, M., et al. 2010, MNRAS, 409, 48
Rowan-Robinson, M. 2001, ApJ, 549, 745
Sanders, D. B., & Mirabel, I. F. 1996, ARA&A, 34, 749
Sanders, D. B., Salvato, M., Aussel, H., et al. 2007, ApJS, 172, 86
Santini, P., Maiolino, R., Magnelli, B., et al. 2010, A&A, 518, L154
Scoville, N., Aussel, H., Brusa, M., et al. 2007, ApJS, 172, 1
Shao, L., Lutz, D., Nordon, R., et al. 2010, A&A, 518, L26
Shapiro, K. L., Genzel, R., Förster Schreiber, N. M., et al. 2008, ApJ, 682, 231
Soifer, B. T., Helou, G., & Werner, M. 2008, ARA&A, 46, 201
Starck, J., & Murtagh, F. 1998, PASP, 110, 193
Tran, K. H., Kelson, D. D., van Dokkum, P., et al. 1999, ApJ, 522, 39
Wieprecht, E., Schreiber, J., de Jong, J., et al. 2009, ADASS XVIII, ed. D. Bohlender, D. Durand, & P. Dowler, ASP Conf. Ser., 411, 531